Japan Journal of Research

Original Article

Moho Depth and Crustal Velocity Structure Beneath Stations RTC and TAM from Teleseismic Receiver-Function Analysis

Eloumala Onana Parfait Noel[1,3], Iben Brahim Aomar[2], El Mouraouah Azelarab[2] and Chabane Abdelkader[3]

[1]University Institute of technology, Douala University, BP 8698, Douala Cameroon
[2]National institute of Geophysics, CNRST B.P. 8027 Agdal-NU, Rabat Morocco.
[3]Science faculty of the IBN Tofail University, B.P. 133, Kénitra, Morocco.

Correspondence

Eloumala Onana Parfait Noel

Douala University, BP 8698, Douala Cameroon

Tel:+237672476212

Email:parfaitnoele@yahoo.fr

- Received Date: 25 Aug 2024
- Accepted Date: 28 Sep 2024
- Publication Date: 02 Oct 2024

Keywords

Crust, Moho, Station, Velocity model.

Abstract

We apply the P-wave receiver-function technique to invert teleseismic data to investigate the S- wave velocity structure beneath stations RTC and TAM in West Africa. Teleseismic waveform receiver function analysis is a widely used technique for studying crustal structure beneath broadband seismic stations. Our results show that the crust beneath RTC is relatively complex with large velocity fluctuations. In the upper crust, a low velocity layer extends from 8 to 12 km deep. At Tamanrasset crustal structure east and west of the station differ. We find a high-velocity zone between 2 and 8 km to the east that we attribute to a high conductivity unit corresponding to intrusions described in the literature. We find no similar feature west of the station. Our velocity models for RTC and TAM are consistent with their differing tectonic environments. TAM, on a stable craton, displays a fairly homogeneous velocity structure while RTC, on thick sediments in an ocean-continent transition zone, has more heterogeneous structure. This structural difference is reflected as well by the depth to Moho, ~20 km at RTC and nearly 38 km at TAM, although both have gradational velocity increases with depth.

Introduction

Depth to Moho is an important parameter for characterizing crustal structure and often can be related to the geo-tectonic evolution of a given region. The Moho (Mohorovičić discontinuity) that separates the Earth's crust from the underlying mantle is characterized by major changes in seismic velocity, chemical composition, and rheology [1].

In this study of the Rabat, Morocco, and Tamanrasset, Algeria, areas we investigate the crustal structure underneath stations RTC and TAM (Figure 1). Previous studies provide geophysical and geological information about each region. We invert teleseismic seismograms by the method of receiver function analysis, an excellent tool for characterizing seismic discontinuities in the crust by analysis of *P*-to-*S* conversions at the Moho and other velocity discontinuities [2]. The analysis of teleseismic receiver functions has been particularly useful in large-scale structural studies (e.g., using body waves) to determine average crustal velocities because the timing and amplitude of *Ps* conversions provide good constraints on the depths and velocity contrasts of major crustal and upper mantle discontinuities[3,4]. Moho depth is obtained from the *Ps–P* times by adjusting the thickness of the crust and its velocity.

In this paper, we apply the *P*-wave receiver function analysis, which is the most commonly used approach largely for two reasons: *P* is easy to identify and the source and path effects can be removed through a simple deconvolution process with the early part of the vertical component's waveform as the Green's function [5]. Our results include Moho depth and crustal shear wave velocity models, VS, underneath RTC and TAM. Importantly, it is the first study applying the receiver function method to data recorded on RTC where crustal structure provides important constraints on the tectonic evolution of the Atlantic margin around Rabat. There, the stratigraphic transition and tectono-sedimentary subsidence are documented incompletely.

While the Rabat station RTC began operation only in 2002, TAM has been in operation for nearly 28 years, amassing an important database. Although the receiver function method has been applied to TAM, that work used a limited data set ending in 1995 and obtained VS structure that is an average of the structure across all available station-to-source backazimuths; we use a much larger database and invert for velocity structure for several seismic-source clusters lying at different backazimuths and thereby yielding information on lateral variations in structure near the

Citation: Eloumala OPN, Iben BA, El Mouraouah A, Chabane A. Moho Depth and Crustal Velocity Structure Beneath Stations RTC and TAM from Teleseismic Receiver-Function Analysis. Japan J Res. 2024;5(9):68

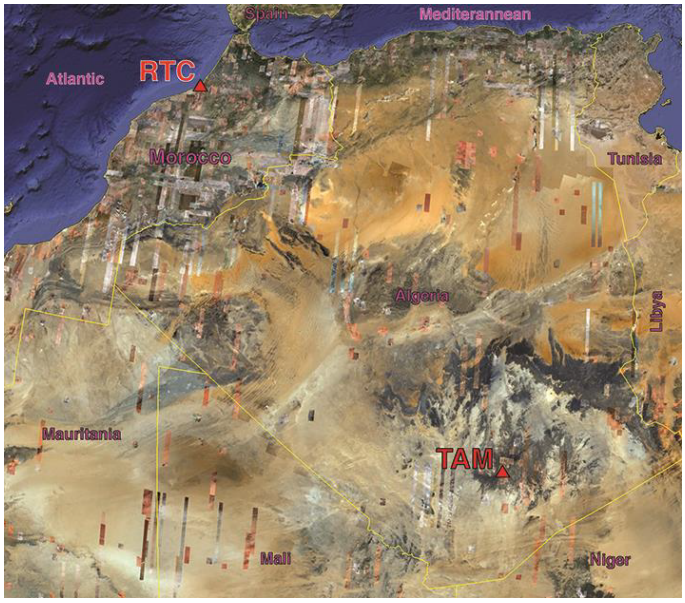

Figure 1. *Map showing stations RTC in Morocco and TAM in Algeria.*

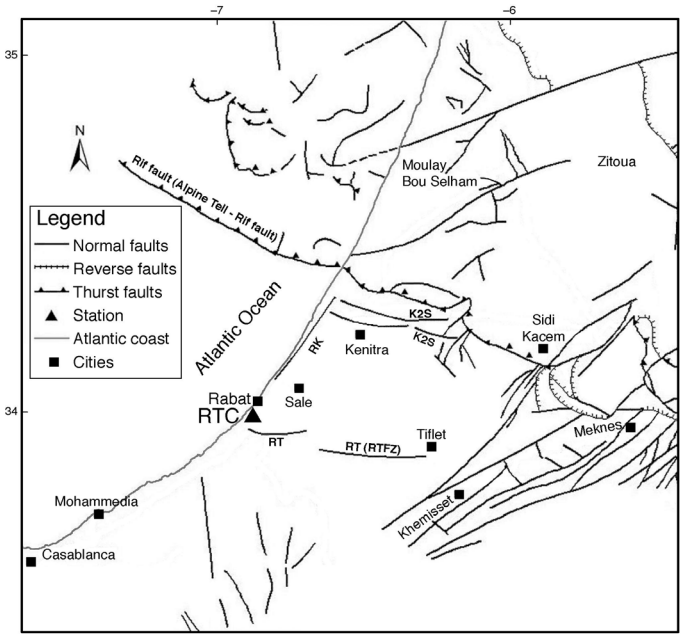

Figure 2. *Location of Hercynian structures; ARK: Rabat-Kenitra fault, K2S: Kenitra-Sidi-Slimane fault and RT (RTFZ): Rabat-Tiflet fault zone.*

stations [6]. As importantly, we compare the velocity structure beneath RTC, which is located in a coastal transition on recent thick sediment, to those obtained for TAM, which is installed on the old crust of the Hoggar Dome.

Geological setting

Geological setting of the Rabat region

Station RTC is installed in the city of Rabat in the Rharb basin; the basin is bounded by two geological domains. To the north lies the Rif, a complex, unstable alpine structure, while to the south is the Hercynian-age (400 to 245 million years ago) western Meseta, believed to be rigid and stable; Atlantic oceanic crust lies to the west. The crustal structure of the Rharb Basin region is characterized by a thick accumulation of sediments Neogene and Quaternary sediment thickness of 5.5 km [7]. The region between Rabat and Tiflet to the east has Paleozoic basement and an angular discordance from there to Miocene- and Moghrabian-age (5 to 2.5 million years ago) deposits [8].

The Rabat area is controlled by northeast-striking normal faults (Figure 2). The Rharb basin is divided by the northwest-striking Tell-Rif fault, a reverse fault. The Tell-Rif forms the south front of the Rif Mountains and extends to the Tell in Algeria (folded coastal massifs and plateaus). These faults are of Hercynian (or "Variscan") age or greater and affect the Paleozoic basement, control the paleogeography of the region, and suggest block tectonics that would explain the shifting between the Plio-Quaternary units [9,10]. The parallel northeast-striking faults extend west to the Atlantic coast and are found again in central Meseta [11;12]. The K2S (Kenitra-Sidi-Slimane) fault strikes N110°E then to the east bends to N90°E); it dips fairly steeply and is located south of the pre-Rif front (Figure 2). The K2S resulted from progressive collapse of the post-Paleozoic northern block of recent deposits in the South Rharb basin. The RTFZ (Rabat-Tiflet fault zone) strikes N80°E to E30°S and forms the meridional border of the Sehoul zone with the Meseta [13].

A velocity model obtained from mining blasts at Khouribga emphasizes three main reflected phases in the Meseta along a profile between Khouribga and Rabat [14]. Two of these are intra-crustal and the third is the Moho reflected wave, *PmP*. These data imply a first layer with VP = 5.8 km/s and a thickness of 15.5 km, a second layer with VP = 6.8 km/s and a thickness of 14 km, and VP = 7.46 km/s below a Moho depth of 29.5 km. We therefore use as our starting model an average crustal thickness of 30 km in the western Moroccan Meseta, with this thickness decreasing toward the coast.

Geological setting of the Tamanrasset region

The Tamanrasset region, where TAM is sited, is in southern Algeria in the Hoggar volcanic area in the central Sahara. Hoggar volcanic area comprises a large portion of the Tuareg shield (Figure 3), which comprises Achaean, Palaeoproterozoic, and Neoproterozoic terrains [15]. The Precambrian meso-catazonal

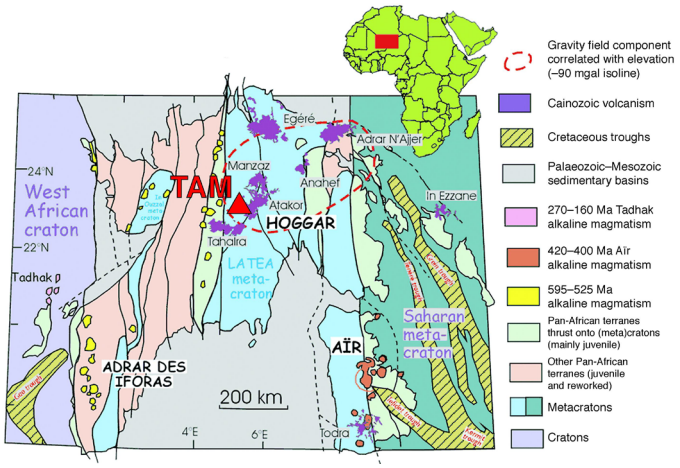

Figure 3: *The Tuareg shield, showing its major terrains [15]*

series making up Hoggar Dome was deformed during the pan-African orogeny (600– 500 Ma); this orogeny generated the pan-African mountain range as a result of convergence between the East African Craton and Hoggar Dome paleocontinent. The pan-African orogeny was controlled by deep tectonic subsidence. Topographic relief in the area probably results from motions on north- south faults dividing the Tuareg shield from the pan-African Shield [16].

More recent volcanism in the Hoggar ranges from Eocene to Quaternary; some authors consider this Cenozoic volcanism the produce of a mantle plume [17]. If so, it may be linked to the Africa- Europe collision by rejuvenation of intra-plate Pan-African structures [15].

On the basis of free-air gravity data, Lesquer et al proposed that the central Hoggar area is underlain by anomalously low-density mantle, he therefore inferred a magmatic body shallower than about 60 km [18]. From the analyzis of the shape of this gravity anomaly, it appears to be correlated with depth to basement, and suggested that the putative magmatic body lies between 20 and 70 km depth and has a maximum thickness of 30 km [18]. The Hoggar region also exhibits a positive free-air gravity anomaly [19]. The association between a low gravity anomaly and Cenozoic volcanism led to suggest that a mantle plume underlies the Hoggar region [20,21]. It suggested that small-sized high- temperature mantle bodies intrude the crust there, beneath the recent volcanic areas [22].

Through integrated analysis of seismic and geologic data, it is suggested that Hoggar crustal thickness is about 38 km and that the inferred mantle anomaly is relatively small (200–300 km wide and less than 60 km in vertical extent) compared to mantle anomalies associated with other hot spots and rift zones [23]. Given the seismic and heat flow data, it is proposed that the mantle beneath the centre of Hoggar volcanic area is intermediate between a cratonic and activated mantle [24]. Low *P*- wave velocities have been found beneath the central Hoggar, extending from the surface down to about 300 km [22]. The largest low-temperature anomaly is thought, in contrast, to be to the north, below the Saharan basins [25]. If at anomaly is related is real, it must have been emplaced before 60 Ma in order to have cooled off [18].

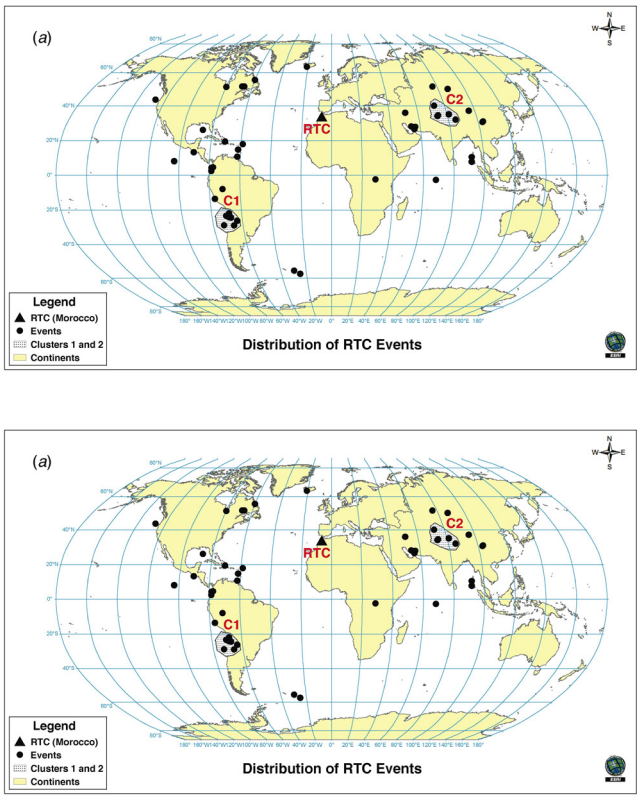

Figure 4. *The Tuareg shield, showing its major terrains [15]*

Data and method

Teleseismic records from the RTC and the TAM are our primary data. RTC is a very broadband station installed in 2002 at latitude 33.99N, longitude 6.86W, and elevation 50 m in Rabat and is part of the Morocco National Seismic Network operated by the National Institute of Geophysics and of Mednet (network code MN), which spans three Mediterranean nations and five institutions. TAM was installed in 1995 in southern Algeria at latitude 22,791, longitude 5,527, and elevation 1377 m; it is part of the GEOSCOPE seismic network. For both stations, epicentral distance (Δ) for the events we use range between 35° and 95° (Tables 1 and 2). In this distance interval, body *P* and other body-wave phases are nearly perfect plane waves and easily modeled. Below 35° distance, ray triplication complicates the wavefronts while over 95° they are muddied by core diffractions. Our waveform data were in SEED format that we read into our programs with routine rdseed. The time window we used from each seismogram starts 5 *s* prior to the *P*-wave onset and ends 40 seconds thereafter. This window includes the *Ps* and the more complex conversions of interest from the crust and the upper mantle. Each event has magnitude mb ≥ 5.6 (Tables 1 and 2 and Figure 4) and waveforms characterized by a clear *P*-wave onset. Finally, our deconvolution must reproduce at least 70% of the signal successfully. Source parameters of these events were obtained from the Wilber II site of IRIS (Incorporated Research Institutions for Seismology).

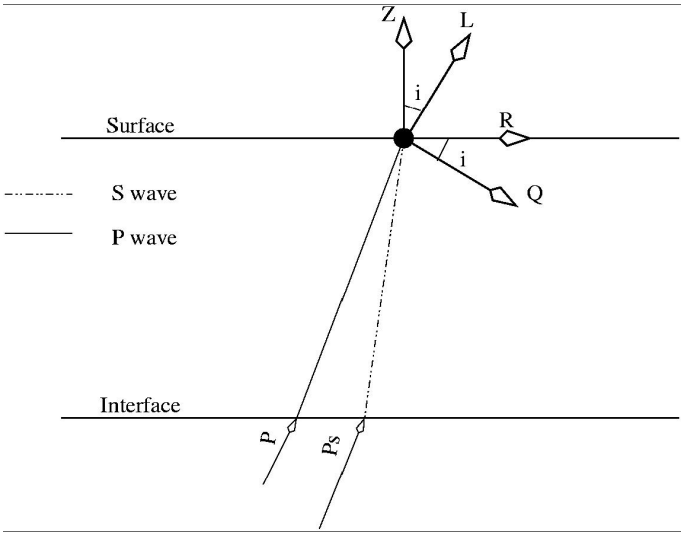

Figure 5. *TSketch showing the Earth-oriented coordinate system (E, N, Z) rotated in to (R, T, Z) and then to (Q, T, L); the coordinate frame of direct P. Component L is in the direction of incident P and largely isolates it from converted phases; Q approximates the direction of SV and the perpendicular to the Figure the direction of* S_H.

Table 1. *Parameters of teleseismic events used to create receiver functions and velocity models for RTC.*

Parameters were taken from IRIS (Incorporated Research Institution for Seismology)

Ev #	Filename	Date (y/m/d)	Origin Time	Lat (°)	Lon (°)	Depth (km)	M	Δ (km)	Azimuth	Back Azm
1	R.RTCBHZ20031070048.1.0	2003/04/17	00:48:30.8	37.53	96.48	14	6.4	8816.431	304.6435	51.92241
2	R.RTCBHZ20031340603.1.0	2003/05/14	06:03:35.8	18.27	–58.63	41	6.6	5400.938	60.55046	264.7747
3	R.RTCBHZ20031672208.1.0	2003/06/16	22:08:02.1	55.49	–160	174	6.9	9766.25	22.06164	345.0914
4	R.RTCBHZ20031710619.1.0	2003/06/20	06:19:38.9	–7.61	–71.72	558	7.1	8227.896	51.51352	249.0483
5	R.RTCBHZ20031741212.1.0	2003/06/23	12:12:35.7	51.58	–167.6	30	6.9	10341.96	15.87166	348.1482
6	R.RTCBHZ20031911706.1.0	2003/07/10	17:06:37.6	28.36	54.17	10	5.8	5766.542	292.4404	78.62715
7	R.RTCBHZ20031962027.1.0	2003/07/17	20:27:50.2	–2.56	68.3	10	7.6	8809.036	305.1412	100.5167
8	R.RTCBHZ20032650446.1.0	2003/09/22	04:45:36.2	19.78	–70.67	10	6.5	6431.921	61.74802	273.2689
9	R.RTCBHZ20032740103.1.0	2003/10/01	01:03:25.2	50.21	87.72	10	6.7	7492.134	296.2435	43.91381
10	R.RTCBHZ20032950230.1.0	2003/10/22	02:30:37.2	8.2	–102.9	10	5.6	10064.48	55.71421	280.1432
11	R.RTCBHZ20033290443.1.0	2003/11/25	04:43:36.8	–23.37	–67.55	160	5.6	9028.163	47.16551	234.1959
12	R.RTCBHZ20041491238.1.0	2004/05/28	12:38:44.2	36.25	51.62	17	6.3	5253.761	285.3203	69.76504
13	R.RTCBHZ20042200930.1.0	2004/08/07	09:30:16.9	51.75	–166.3	8	6.0	10297.3	16.97498	347.3828
14	R.RTCBHZ20042501242.1.0	2004/09/06	12:42:59.3	–55.37	–28.98	10	6.8	10123.3	18.2376	192.4165
15	R.RTCBHZ20042511153.1.0	2004/09/07	11:53:06.2	–28.58	–65.83	22	6.3	9300.811	45.76666	229.3251
16	R.RTCBHZ20043002253.1.0	2004/10/26	22:53:07.8	–57.07	–24.68	10	6.2	10228.88	14.7419	189.6293
17	R.RTCBHZ20043200906.1.0	2004/11/15	09:06:56.5	4.7	–77.51	15	7.1	7939.477	55.82976	262.9619
18	R.RTCBHZ20052051542.1.0	2005/07/24	15:42:06.2	7.92	92.19	16	7.3	10350.87	304.7429	78.42248
19	R.RTCBHZ20052810350.1.0	2005/10/08	03:50:38.6	34.43	73.54	10	7.6	7190.071	294.9949	64.37566
20	R.RTCBHZ20052811046.1.0	2005/10/08	10:46:28.7	34.73	73.74	8	6.4	7192.581	294.9466	63.99848
21	R.RTCBHZ20053311022.1.0	2005/11/27	10:22:23.5	26.84	55.83	35	6.1	5983.553	293.8224	79.6481
22	R.RTCBHZ20060590731.1.0	2006/02/28	07:31:02.6	28.12	56.87	18	6.0	6021	293.1815	77.74673
23	R.RTCBHZ20061650418.1.0	2006/06/14	04:18:42.5	51.75	177.24	14	6.4	10497.67	3.413951	357.4464
24	R.RTCBHZ20061792102.1.0	2006/06/28	21:02:09.2	26.82	55.9	10	5.8	5990.812	293.8487	79.63937
25	R.RTCBHZ20061892040.1.0	2006/07/08	20:40:00.9	51.21	–179.3	22	6.6	10537.33	6.288139	355.2437
26	R.RTCBHZ20061971142.1.0	2006/07/16	11:42:41.4	–28.72	–72.54	10	6.2	9795.322	49.25521	233.2148
27	R.RTCBHZ20062531456.1.0	2006/09/10	14:56:07.8	26.34	–86.57	10	5.8	7533.292	62.04618	287.4481
28	R.RTCBHZ20062721308.1.0	2006/09/29	13:0826.1	10.88	–61.76	53	6.1	6118.764	56.09073	258.8477
29	R.RTCBHZ20062800820.1.0	2006/10/07	08:20:57.1	–23.99	–68.43	104	5.8	9140.707	47.53061	234.2896
30	R.RTCBHZ20062931048.1.0	2006 /10/20	10:48:56.0	–13.46	–76.68	23	6.7	9054.769	52.07698	247.4653
31	R.RTCBHZ20063111325.1.0	2006/11/07	13:25:36.9	–21.73	–68.26	125	5.6	8959.123	47.70243	235.8634
32	R.RTCBHZ20063170126.1.0	2006/11/13	01:26:34.0	–26.08	–63.29	550	6.8	8927.278	44.63107	229.5011
33	R.RTCBHZ20063561950.1.0	2006/12/22	19:50:44.6	10.65	92.36	24	6.3	10193.24	304.8654	76.0974
34	R.RTCBHZ20070770211.1.0	2007/03/18	02:11:05.9	4.58	–78.49	10	6.3	8036.867	55.89882	263.4351
35	R.RTCBHZ20071451747.1.0	2007/05/25	17:47:31.2	–24.22	–67.03	180	5.9	9053.612	46.81148	233.2412
36	R.RTCBHZ20071641929.1.0	2007/06/13	19:29:40.1	13.55	–90.62	23	6.5	8614.771	57.80031	277.929
37	R.RTCBHZ20072140321.1.0	2007/08/02	03:21:46.5	51.36	–179.9	48	6.9	10525.26	5.771432	355.6481
38	R.RTCBHZ20072272340.1.0	2007/08/15	23:40:56.8	–13.36	–76.52	30	8.0	9034.3	52.03745	247.4477
39	R.RTCBHZ20072530149.1.0	2007/09/10	01:49:10.5	2.91	–78.15	8.8	6.9	8110.046	55.43046	261.7987
40	R.RTCBHZ20073331900.1.0	2007/11/29	19:00:19.2	14.92	–61.26	145	7.3	5831.094	58.49063	262.7127
41	R.RTCBHZ20073470723.1.0	2007/12/13	07:23:46.5	–23.01	–70.34	58	6.2	9213.241	48.53911	236.2039
42	R.RTCBHZ20080010632.1.0	2008/01/01	06:32:13.8	40.39	72.91	23	6.2	6873.9	291.962	58.48932
43	R.RTCBHZ20080090826.1.0	2008/01/09	08:26:45.9	32.29	85.17	10	6.4	8257.53	300.3865	61.56149
44	R.RTCBHZ20080090827.1.0	2008/01/09	08:26:45.9	32.27	85.24	10	6.3	8264.337	300.4201	61.54818

Ev #	Filename	Date (y/m/d)	Origin Time	Lat (°)	Lon (°)	Depth (km)	M	Δ (km)	Azimuth	Back Azm
45	R.RTCBHZ20080100137.1.0	2008/01/10	01:37:18.5	43.78	–127.3	10	6.3	9495.834	45.94913	321.2047
46	R.RTCBHZ20080161154.1.0	2008/01/16	11:54:41.7	32.39	85.23	23	6.2	8256.766	300.387	61.44543
47	R.RTCBHZ20080340734.1.0	2008/02/03	07:34:12.2	–2.31	28.9	10	6.3	5491.543	320.2117	129.6832
48	R.RTCBHZ20080802232.1.0	2008/03/20	22:32:57.9	35.49	81.47	10	6.3	7785.416	297.9172	60.20974
49	R.RTCBHZ20080802233.1.0	2008/03/20	22:33:00.0	35.44	81.39	22	6.3	7781.613	297.8981	60.28918
50	R.RTCBHZ20081330628.1.0	2008/07/12	06:28:00.8	31.08	103.27	10	6.3	9745.216	308.6671	53.73045
51	R.RTCBHZ20081330643.1.0	2008/07/12	06:43:14.8	31.25	103.68	10	6.3	9763.779	308.8644	53.37799
52	R.RTCBHZ20081501546.1.0	2008/12/23	15:46:01.3	64.03	–20.99	10	6.3	3478.947	157.0211	348.0612

Table 1.1 *Events used to create "velocity model a" from Cluster 1 for RTC.*

Filename	date	O. Time	Lat	Lon	depth	Mag	Δ (km)	Azimuth	Back Azm
R.RTCBHZ20080340734.1.0	2008/02/03	07:34:12.2	–20.02	–69.84	10	6.3	8955.394	48.6398	238.148
R.RTCBHZ20063111325.1.0	2006/11/07	13:25:36.9	–21.73	–68.26	125	5.6	8959.123	47.70243	235.8634
R.RTCBHZ20073470723.1.0	2007/12/13	07:23:46.5	–23.01	–70.34	58	6.2	9213.241	48.53911	236.2039
R.RTCBHZ20033290443.1.0	2003/11/25	04:43:36.8	–23.37	–67.55	160	5.6	9028.163	47.16551	234.1959
R.RTCBHZ20062800820.1.0	2006/10/07	08:20:57.1	–23.99	–68.43	104	5.8	9140.707	47.53061	234.2896
R.RTCBHZ20071451747.1.0	2007/05/25	17:47:31.2	–24.22	–67.03	180	5.9	9053.612	46.81148	233.2412
R.RTCBHZ20063170126.1.0	2006/11/13	01:26:34.0	–26.08	–63.29	550	6.8	8927.278	44.63107	229.5011
R.RTCBHZ20042511153.1.0	2004/09/07	11:53:06.2	–28.58	–65.83	22	6.3	9300.811	45.76666	229.3251
R.RTCBHZ20061971142.1.0	2006/07/16	11:42:41.4	–28.72	–72.54	10	6.2	9795.322	49.25521	233.2148

Table 1.2 *Events used to create "velocity model b" from Cluster 2 for RTC.*

Filename	date	O. Time	Lat	Lon	depth	Mag	Δ (km)	Azimuth	Back Azm
R.RTCBHZ20080802233.1.0	2008/03/20	22:33:00.0	35.44	81.39	22	6.3	7781.613	297.8981	60.28918
R.RTCBHZ20080802232.1.0	2008/03/20	22:32:57.9	35.49	81.47	10	6.3	7785.416	297.9172	60.20974
R.RTCBHZ20080090826.1.0	2008/01/09	08:26:45.9	32.29	85.17	10	6.4	8257.53	300.3865	61.56149
R.RTCBHZ20080161154.1.0	2008/01/16	11:54:41.7	32.39	85.23	23	6.2	8256.766	300.387	61.44543
R.RTCBHZ20080090827.1.0	2008/01/09	08:26:45.9	32.27	85.24	10	6.3	8264.337	300.4201	61.54818
R.RTCBHZ20052810350.1.0	2005/10/08	03:50:38.6	34.43	73.54	10	7.6	7190.071	294.9949	64.37566
R.RTCBHZ20052811046.1.0	2005/10/08	10:46:28.7	34.73	73.74	8	6.4	7192.581	294.9466	63.99848
R.RTCBHZ20080010632.1.0	2008/01/01	06:32:13.8	40.39	72.91	23	6.2	6873.900	291.962	58.48932
R.RTCBHZ20061971142.1.0	2006/07/16	11:42:41.4	–28.72	–72.54	10	6.2	9795.322	49.25521	233.2148

Procedure for Receiver Functions determination

After selecting and windowing waveforms, receiver function extraction is in essential steps, rotating the components into the *P*-wave coordinate frame and isolating the receiver function from other effects.

Converted phases from teleseismic *P* can be interpreted in terms of Earth structure by the receiver- function technique. Langston proposed a version of this technique for isolating shallow-structure effects from the early portion of the *P* coda [2]. Presently, a variety of receiver function techniques have been developed. In this work, we use the method and software developed by Herrmann, which allows us to generate images of both the crust and upper mantle velocity structure in some detail by iterative waveform fitting [26].

To separate converted *S*-phases from direct *P,* we rotate each record from its original (Z, N, E) components into the coordinates of the *P* wavefront and propagation directions; we call these rotated components (L, Q, R), as shown in Figure 5. The L-component is oriented in the direction of direct *P,* while orthogonal components Q and R should be about parallel to SV and SH particle motions, so seismograms rotated into (L, Q, R) will show mainly *P, SV,* and *SH* phases [27]. Rotation is performed, therefore, using both the backazimuth and the incidence angle of the incoming *P* wave at the station, with backazimuth and incidence angle estimated from hypocentral and station coordinates. In theory, this transformation nearly isolates the *P* displacement on the *L*-component and the SH displacement on T, whereas the *SV* displacement is mainly isolated on the Q component. Thus, *L* serves as a Green's function to deconvolve unwanted portions of the signal from converted phases in Q, while *T* serves to help evaluate error since in simple models it will be zero until direct *S* arrives.

Within the Earth, incoming *P* undergoes a convolution with velocity structure. Receiver function analysis extracts the

Table 2. *Parameters of teleseismic events used to create receiver functions and velocity models for TAM.*

Parameters were taken from IRIS (Incorporated Research Institution for Seismology)

Ev#	Filename	Date	Orig. Time	M	Depth	Lat	Lon	Δ (km)	Azimuth	Back Azm
1	R.TAMBHZ20090651050.1.0	2009 /03/06	10:50:29.4	6.4	9	80.32	–1.85	6409.213	171.9406	358.5267
2	R.TAMBHZ20002760225.1.0	2000 /10/02	02 :25 :31.3		34	–7.08	30.71	4294.61	320.9768	137.3795
3	R.TAMBHZ20072021327.1.0	2007/07/21	13 :27 :08.9	6.1	632.9	–7.98	–71.13	9006.512	65.41331	257.4057
4	R.TAMBHZ20081742356.1.0	2008/06/22	23 :56 :30.0	6.1	18	67.7	141.28	9334.773	319.6533	15.52958
5	R.TAMBHZ20032160437.1.0	2003 /08/04	04 :37 :20.1	7.5	10	–60.53	–43.41	10233.89	44.1264	201.9043
6	R.TAMBHZ20053141929.1.0	2005/11/10	19 :29 :54.1	5.9	6	57.47	120.99	9299.079	303.0424	29.39248
7	R.TAMBHZ20050821359.1.0	2005/03/23	13 :59 :17.0	5.8	10	–55.48	–1.54	8698.055	6.660978	184.1032
8	R.TAMBHZ20032740103.1.0	2003/10/01	01 :03 :25.2	6.7	10	50.21	87.72	7551.082	279.4033	43.38296
9	R.TAMBHZ20032701852.1.0	2003/09/27	18 :52 :49.9	6.4	10	50.09	87.77	7556.823	279.4874	43.50512
10	R.TAMBHZ20003301809.1.0	2000/11/25	18 :09 :11.4	6.3	50.4	40.25	49.95	4582.586	258.6725	54.40956
11	R.TAMBHZ20052190217.1.0	2005/08/07	02 :17 :46.0	6.2	10	–4.7	33.62	4311.097	316.0087	131.3994
12	R.TAMBHZ20043200906.1.0	2004/11/15	09 :06 :56.5	7.1	15	4.7	–77.51	9101.759	67.7491	271.6545
13	R.TAMBHZ20070770211.1.0	2007/03/18	02 :11 :25.9	6.3	10	4.58	–78.59	9217.637	67.70253	271.9549
14	R.TAMBHZ20082791552.1.0	2008/10/05	15 :52 :49.4	6.6	27.4	39.53	73.82	6611.889	275.4299	56.54097
15	R.TAMBHZ20070950356.1.0	2007/04/05	03 :56 :35.7	6.3		37.38	–24.62	3304.524	110.7514	306.1781
16	R.TAMBHZ20040110432.1.0	2004/01/11	04 :32 :47.7	6.2	5.30	–36.7	53.35	8280.208	314.7626	141.804
17	R.TAMBHZ20050472027.1.0	2005/02/16	20 :27 :52.4	6.6	10	–36.32	–16.56	6942.826	23.05433	200.0418
18	R.TAMBHZ20041491238.1.0	2004/05/28	12 :38 :44.2	6.3	17	36.25	51.62	4662.386	264.3792	60.65666
19	R.TAMBHZ20010990900.1.0	2001/04/09	09 :00 :57.1	6.7	11	–32.67	–73.11	10357.51	64.96644	235.9032
20	R.TAMBHZ20001140927.1.0	2000/04/23	09 :27 :23.3	7.0	608.5	–28.31	–62.99	9273.256	59.83707	235.6968
21	R.TAMBHZ20001701444.1.0	2000/06/18	14 :44 :13.3	7.8	10	–13.8	97.45	10793.18	291.6897	101.9887
22	R.TAMBHZ20090331753.1.0	2009/02/02	17 :53 :21.8	6.0	21	–13.58	–76.56	9802.475	66.14616	254.5124
23	R.TAMBHZ20032232122.1.0	2003/08/11	21 :22 :30.4	6.0	100	12.12	93.53	9299.907	291.8584	79.5996
24	R.TAMBHZ20081791140.1.0	2008/06/27	11 :40 :01.1	6.7	35	11.03	91.91	9180.917	291.73	81.20659
25	R.TAMBHZ20081801254.1.0	2008/06/28	12 :54 :46.3	6.1	15	10.85	91.71	9168.024	291.724	81.44757
26	R.TAMBHZ20052051542.1.0	2005/07/24	15 :42 :06.2	7.3	16	7.92	92.19	9338.387	292.1048	83.98985
27	R.TAMBHZ20083150122.1.0	2008/11/10	01 :22 :01.1	6.4	10	37.62	95.85	8528.534	288.5126	54.67771
28	R.TAMBHZ20082180949.1.0	2008/08/05	09 :49 :17.9	6.0	10	32.81	105.56	9546.345	294.3392	56.24513
29	R.TAMBHZ20081330629.1.0	2008/05/12	06 :28 :01.5	7.9	19	31	103..32	9434.431	293.3578	58.6737
30	R.TAMBHZ20071532134.1.0	2007/06/02	21 :34 :33.3	6.1	5	23.03	101.05	9577.173	292.972	66.7937
31	R.TAMBHZ20081330628.1.0	2008/05/12	06 :28 :00.8	7.5	10	31.08	103.27	9426.517	293.3271	58.61726
32	R.TAMBHZ20081340707.1.0	2008/05/13	07 :07 :09.0	5.9	10	30.94	103.25	9430.951	293.3292	58.75276
33	R.TAMBHZ20081501546.1.0	2008/05/29	15 :46 :00.4	6.2	10	64	–21.01	4978.562	144.184	343.7706
34	R.TAMBHZ20001730058.1.0	2000/06/21	00 :51 :46.8	6.5	10	63.98	–20.76	4969.611	144.4869	343.8811
35	R.TAMBHZ20001691540.1.0	2000/06/17	15 :40 :41.7	6.5	10	63.97	–20.49	4961.047	144.8216	344.011
36	R.TAMBHZ20032650445.1.0	2003/09/22	04 :45 :36.2	6.5	10	19.78	–70.67	7822.446	72.14728	283.7575
37	R.TAMBHZ20082851040.1.0	2008/10/11	10 :40 :14.9	6.1	29.30	19.15	–64.81	7256.243	73.17117	281.3322
38	R.TAMBHZ20073331900.1.0	2007/11/29	19 :00 :07.4	7.4	147.5	14.97	–61.26	7035.557	71.7981	275.7964
39	R.TAMBHZ20010260316.1.0	2001/01/26	03 :16 :40.5	7.7	16	23.42	70.23	6568.052	283.3467	75.5798
40	R.TAMBHZ20083022309.1.0	2008/10/28	23 :09 :57.6	6.4	15	30.64	67.37	6140.417	277.7774	67.72042
41	R.TAMBHZ20083031132.1.0	2008/10/29	11 :32 :431	6.4	14	30.6	67.46	6149.573	277.8431	67.75567
42	R.TAMBHZ20052811046.1.0	2005/10/08	10 :46 :28.7	6.4	8	34.73	73.1	6610.842	277.8468	62.14484
43	R.TAMBHZ20083602240.1.0	2008/12/25	22 :40 :23.6	5.8	13	23.4	64.5	5997.161	281.8557	76.98015
44	R.TAMBHZ20090591433.1.0	2009/02/28	14 :33 :06.0	6.3	10	–60.39	–24.86	9621.792	27.88403	194.5764
45	R.TAMBHZ20032730801.1.0	2003/09/30	08 :01 :33.1	6.0	10	–60.32	–33.4	9862.899	35.4512	198.2271

Ev#	Filename	Date	Orig. Time	M	Depth	Lat	Lon	Δ (km)	Azimuth	Back Azm
46	R.TAMBHZ20091061457.1.0	2009/04/16	14 :57 :06.1	6.7	20	–60.02	–26.86	9639.151	29.67982	195.6324
47	R.TAMBHZ20011031533.1.0	2001/04/13	15 :33 :53.5	6.2	26	–59.72	–25.59	9575.301	28.55704	195.2183
48	R.TAMBHZ20081191557.1.0	2008/04/28	15 :57 :55.2	6.1	35	–58.74	–24.71	9455.352	27.80733	195.284
49	R.TAMBHZ20081820617.1.0	2008/06/30	06 :17 :44.8	9.0	19	–58.22	–22.1	9335.229	25.49023	194.2878
50	R.TAMBHZ20081050945.1.0	2008/04/14	09 :45 :19.7	6.0	140	–56.02	–28.04	9289.819	30.90026	198.2072
51	R.TAMBHZ20070200621.1.0	2007/01/20	06 :21 :16.3	6.1	10	–55.42	–28.52	9248.278	31.35967	198.7543
52	R.TAMBHZ20070592313.1.0	2007/02/28	23 :13 :25.9	6.2	35	–55.17	–29.18	9246.633	31.95564	199.2104
53	R.TAMBHZ20043492320.1.0	2004/12/14	23 :20 :13.3	6.8	10	18.96	–81.41	8916.818	69.2793	286.4234
54	R.TAMBHZ20091480824.1.0	2009/05/28	08 :24 :45.7	7.1	10	16.78	–86.17	9474.649	67.78043	286.0634
55	R.TAMBHZ20071870109.1.0	2007/07/06	01 :09 :22.2	6.1	124.8	16.68	–93.48	10194.72	65.76115	288.7342
56	R.TAMBHZ20041200057.1.0	2004/04/29	00 :57 :21.0	6.2	10	10.81	–86	9710.636	67.45341	280.5012
57	R.TAMBHZ20090081921.1.0	2009/01/08	19 :21 :35.6	6.1	14	10.17	–84.2	9555.74	67.70341	279.2358
58	R.TAMBHZ20070352056.1.0	2007/02/04	20 :56 :25.9	6.2	10	19.37	–78.52	8616.1	70.11055	285.8469
59	R.TAMBHZ20043250807.1.0	2004/11/20	08 :07 :22.0	6.4	16	9.6	–84.17	9576.741	67.67082	278.6993
60	R.TAMBHZ20002030153.1.0	2000/07/21	01 :53 :35.8	6.4	33	9.42	–85.33	9702.021	67.49638	278.9708
61	R.TAMBHZ20012370202.1.0	2001/08/25	02 :02 :02.5	6.1	24.5	7.63	–82.77	9517.317	67.70744	276.3566
62	R.TAMBHZ20050010625.1.0	2005/01/01	06 :25 :44.8	6.6	11.7	5.1	92.3	9468.105	292.363	86.55355
63	R.TAMBHZ20040351159.1.0	2004/02/04	11 :59 :47.6	6.1	29.2	8.36	–82.88	9497.81	67.74906	277.0714
64	R.TAMBHZ20051061638.1.0	2005/04/16	16 :38 :03.9	6.4	31	1.81	97.66	10157.8	292.715	87.51874
65	R.TAMBHZ20043610058.1.0	2004/12/26	00 :58 :53.4	9.0	30	3.3	95.98	9921.77	292.6432	86.80038
66	R.TAMBHZ20051860152.1.0	2005/07/05	01 :52 :02.9	6.7	21	1.82	97.08	10097.87	292.693	87.73336
67	R.TAMBHZ20072630831.1.0	2007/09/20	08 :31 :15.8	6.7	30	–2	100.14	10575.24	292.5713	90.05944
68	R.TAMBHZ20072552348.1.0	2007/09/12	23 :48 :04.7	7.9	10	–2.67	100.8	10671.49	292.51	90.42296
69	R.TAMBHZ20050452338.1.0	2005/02/14	23 :38 :08.6	6.1	22	41.73	79.44	7056.046	277.626	53.50494
70	R.TAMBHZ20033350138.1.0	2003/12/01	01 :38 :31.9	6.0	10	41.52	80.52	7148.439	278.3873	53.61074
71	R.TAMBHZ20082800830.1.0	2008/10/06	08 :30 :45.6	6.6	10	29.76	90.3	8311.741	287.7058	63.84501
72	R.TAMBHZ20080161154.1.0	2008/01/16	11 :55 :44.2	5.9	9	32.33	85.16	7760.834	284.6728	62.55562
73	R.TAMBHZ20080161155.1.0	2008/01/16	11 :55 :01.2	5.9	11.7	32.32	85.23	7767.49	284.7081	62.54988
74	R.TAMBHZ20080090826.1.0	2008/01/09	08 :26 :45.4	6.4	10	32.29	85.17	7762.878	284.6915	62.59444
75	R.TAMBHZ20050801223.1.0	2005/03/21	12 :23 :54.0	6.9	579.1	–24.98	–63.47	9131.244	60.4482	238.8123
76	R.TAMBHZ20073220540.1.0	2007/11/18	05 :40 :41.7	6.1	166.1	–22.5	–66.2	9243.225	61.98232	242.209
77	R.TAMBHZ20073181540.1.0	2007/11/14	15 :40 :14.8	7.7	40	–22.25	–69.89	9568.588	63.55089	244.0011
78	R.TAMBHZ20072021534.1.0	2007/07/21	15 :34 :29.6	6.3	289.5	–22.15	–65.78	9186.81	61.8394	242.3341
79	R.TAMBHZ20032081141.1.0	2003/07/27	11 :41 :27.0	6.0	345.3	–20.13	–65.19	9027.3	61.84512	243.8618
80	R.TAMBHZ20082862055.1.0	2008/10/12	20 :55 :41.4	6.1	29.3	–20.12	–64.97	9006.499	61.7558	243.7718
81	R.TAMBHZ20091070208.1.0	2009/04/17	02 :08 :06.7	6.3	10	–19.58	–70.42	9487.392	63.93901	246.6105
82	R.TAMBHZ20011801835.1.0	2001/06/29	18 :35 :51.9		273	–19.56	–66.25	9095.939	62.34899	244.8408
83	R.TAMBHZ20011770418.1.0	2001/06/26	04 :18 :31.3	6.8	24	–17.75	–71.65	9516.24	64.50419	248.7637
84	R.TAMBHZ20011742033.1.0	2001/06/23	20 :33 :14.1	8.4	33	–16.27	–73.64	9638.588	65.23079	250.9098
85	R.TAMBHZ20001331843.1.0	2000/05/12	18 :43 :18.1	7.2	225	–23.55	–66.45	9320.418	61.98525	241.3891
86	R.TAMBHZ20081151214.1.0	2008/04/24	12 :14 :49.9	6.4	10	–1.18	–28.47	4540.394	52.16709	238.8319
87	R.TAMBHZ20082242344.1.0	2008/08/11	23 :38 :38.3	6.0	13	–1.02	–21.84	3967.522	46.71233	232.0597
88	R.TAMBHZ20050120840.1.0	2005/01/12	08 :40 :03.6	6.8	10	–0.88	–21.19	3904.419	46.21286	231.4604
89	R.TAMBHZ20071840826.1.0	2007/07/03	08 :26 :58.9	6.1	10	0.72	–30.27	4577.265	55.15508	242.7784
90	R.TAMBHZ20072122255.1.0	2007/07/31	22 :55 :41.7	6.1	10	–0.1	–17.8	3577.252	43.38499	228.1009
91	R.TAMBHZ20081441936.1.0	2008/05/20	17 :08 :02.3	5.6	62.9	7.31	–34.9	4651.211	63.89215	254.8477
92	R.TAMBHZ20081441935.1.0	2008/05/23	19 :35 :35.1	6.4	10	7.26	–34.88	4651.667	63.835	254.7677

Table 2.1. *Events used to create "velocity model (a)" from Cluster 1 for TAM.*

Filename	Date	Orig. Time	Lat	Lon	Depth	M	Δ (km)	Azimuth	Back Azm
R.TAMBHZ20050801223.1.0	2005/03/21	12 :23 :54.0	–24.98	–63.47	579.1	6.9	9131.244	60.4482	238.8123
R.TAMBHZ20073220540.1.0	2007/11/18	05 :40 :41.7	–22.5	–66.2	166.1	6.1	9243.225	61.98232	242.209
R.TAMBHZ20073181540.1.0	2007/11/14	15 :40 :14.8	–22.25	–69.89	40	7.7	9568.588	63.55089	244.0011
R.TAMBHZ20072021534.1.0	2007/07/21	15 :34 :29.6	–22.15	–65.78	289.5	6.3	9186.81	61.8394	242.3341
R.TAMBHZ20032081141.1.0	2003/07/27	11 :41 :27.0	–20.13	–65.19	345.3	6.0	9027.3	61.84512	243.8618
R.TAMBHZ20082862055.1.0	2008/10/12	20 :55 :41.4	–20.12	–64.97	29.3	6.1	9006.499	61.7558	243.7718
R.TAMBHZ20091070208.1.0	2009/04/17	02 :08 :06.7	–19.58	–70.42	10	6.3	9487.392	63.93901	246.6105
R.TAMBHZ20011801835.1.0	2001/06/29	18 :35 :51.9	–19.56	–66.25	273		9095.939	62.34899	244.8408
R.TAMBHZ20011770418.1.0	2001/06/26	04 :18 :31.3	–17.75	–71.65	24	6.8	9516.24	64.50419	248.7637
R.TAMBHZ20011742033.1.0	2001/06/23	20 :33 :14.1	–16.27	–73.64	33	8.4	9638.588	65.23079	250.9098
R.TAMBHZ20001331843.1.0	2000/05/12	18 :43 :18.1	–23.55	–66.45	225	7.2	9320.418	61.98525	241.3891
R.TAMBHZ20081151214.1.0	2008/04/24	12 :14 :49.9	–1.18	–28.47	10	6.4	4540.394	52.16709	238.8319

Table 2.2. *Events used to create "velocity model (b)" from Cluster 2 for TAM..*

Filename	Date	Orig. Time	Lat	Lon	Depth	M	Δ (km)	Azimuth	Back Azm
R.TAMBHZ20083150122.1.0	2008/11/10	01 :22 :01.1	37.62	95.85	10	6.4	8528.534	288.5126	54.67771
R.TAMBHZ20082180949.1.0	2008/08/05	09 :49 :17.9	32.81	105.56	10	6.0	9546.345	294.3392	56.24513
R.TAMBHZ20081330629.1.0	2008/05/12	06 :28 :01.5	31	103..32	19	7.9	9434.431	293.3578	58.6737
R.TAMBHZ20071532134.1.0	2007/06/02	21 :34 :33.3	23.03	101.05	5	6.1	9577.173	292.972	66.7937
R.TAMBHZ20081330628.1.0	2008/05/12	06 :28 :00.8	31.08	103.27	10	7.5	9426.517	293.3271	58.61726
R.TAMBHZ20081340707.1.0	2008/05/13	07 :07 :09.0	30.94	103.25	10	5.9	9430.951	293.3292	58.75276

Table 2.3. *Events used to create "velocity model (c)" from Cluster 3 for TAM.*

Filename	Date	Orig. Time	Lat	Lon	Depth	M	Δ (km)	Azimuth	Back Azm
R.TAMBHZ20043492320.1.0	2004/12/14	23 :20 :13.3	18.96	–81.41	10	6.8	8916.818	69.2793	286.4234
R.TAMBHZ20091480824.1.0	2009/05/28	08 :24 :45.7	16.78	–86.17	10	7.1	9474.649	67.78043	286.0634
R.TAMBHZ20071870109.1.0	2007/07/06	01 :09 :22.2	16.68	–93.48	124.8	6.1	10194.72	65.76115	288.7342
R.TAMBHZ20041200057.1.0	2004/04/29	00 :57 :21.0	10.81	–86	10	6.2	9710.636	67.45341	280.5012
R.TAMBHZ20090081921.1.0	2009/01/08	19 :21 :35.6	10.17	–84.2	14	6.1	9555.74	67.70341	279.2358
R.TAMBHZ20070352056.1.0	2007/02/04	20 :56 :25.9	19.37	–78.52	10	6.2	8616.1	70.11055	285.8469
R.TAMBHZ20043250807.1.0	2004/11/20	08 :07 :22.0	9.6	–84.17	16	6.4	9576.741	67.67082	278.6993
R.TAMBHZ20002030153.1.0	2000/07/21	01 :53 :35.8	9.42	–85.33	33	6.4	9702.021	67.49638	278.9708
R.TAMBHZ20012370202.1.0	2001/08/25	02 :02 :02.5	7.63	–82.77	24.5	6.1	9517.317	67.70744	276.3566

Table 2.4. *Events used to create "velocity model (d)" from Cluster 4 for TAM.*

Filename	Date	Orig. Time	Lat	Lon	Depth	M	Δ (km)	Azimuth	Back Azm
R.TAMBHZ20050010625.1.0	2005/01/01	06 :25 :44.8	5.1	92.3	11.7	6.6	9468.105	292.363	86.55355
R.TAMBHZ20051061638.1.0	2005/04/16	16 :38 :03.9	1.81	97.66	31	6.4	10157.8	292.715	87.51874
R.TAMBHZ20043610058.1.0	2004/12/26	00 :58 :53.4	3.3	95.98	30	9.0	9921.77	292.6432	86.80038
R.TAMBHZ20051860152.1.0	2005/07/05	01 :52 :02.9	1.82	97.08	21	6.7	10097.87	292.693	87.73336
R.TAMBHZ20072630831.1.0	2007/09/20	08 :31 :15.8	–2	100.14	30	6.7	10575.24	292.5713	90.05944
R.TAMBHZ20072552348.1.0	2007/09/12	23 :48 :04.7	–2.67	100.8	10	7.9	10671.49	292.51	90.42296

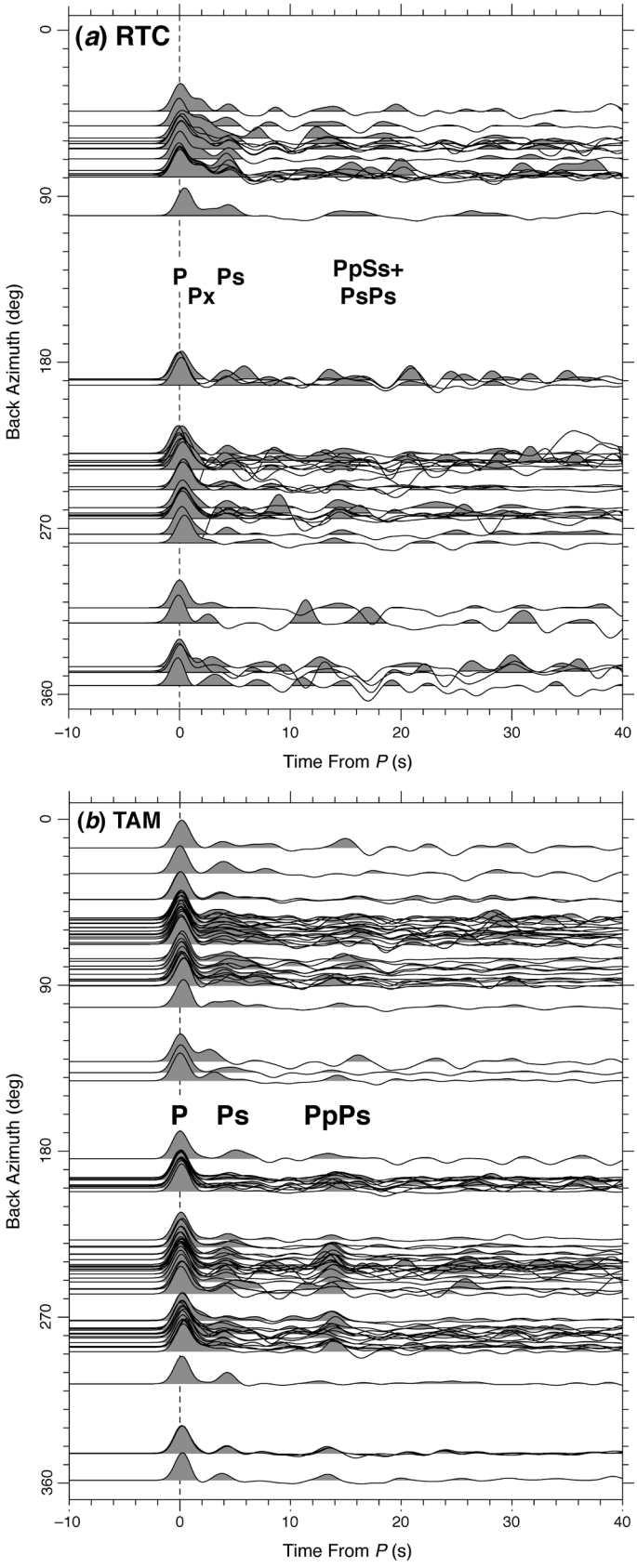

Figure 6. *Receiver functions estimates for (a) RTC and (b) TAM stations. The receiver functions are plotted by backazimuth (BAZ). Gaussian filter parameters 1.0. The Px peak is from an intra-crustal (intermediate) conversion phase. Phases seen consistently include Ps (Moho P-to-S converted phase) and PpPs and PPSS+PSPS (multiples).*

information on the Earth response encoded by this convolution. For an incoming *P* wave, ground displacement can be defined by the convolution of its source function *S(t)*, the instrument response *I(t)* and the transfer function *E(t)* of the path structure between the source and the sensor [28]. Our deconvolution is performed in the time domain and effectively removes most of *S(t)* and *I(t)* along with those portions of *E(t)* common to components L and Q [26]; because most *P*-to-*S* conversions happen at relatively sharp interfaces and these tend to be absent in the lower mantle and because wavefronts heal as they travel, muting the effects of distal interfaces, deconvolving largely isolates the crustal and upper-mantle parts of *E(t)* beneath the seismic station. These conversion coefficients identify and quantify the impedance mismatches among different geological layers in the crust and upper mantle. In the ideal case, the resulting

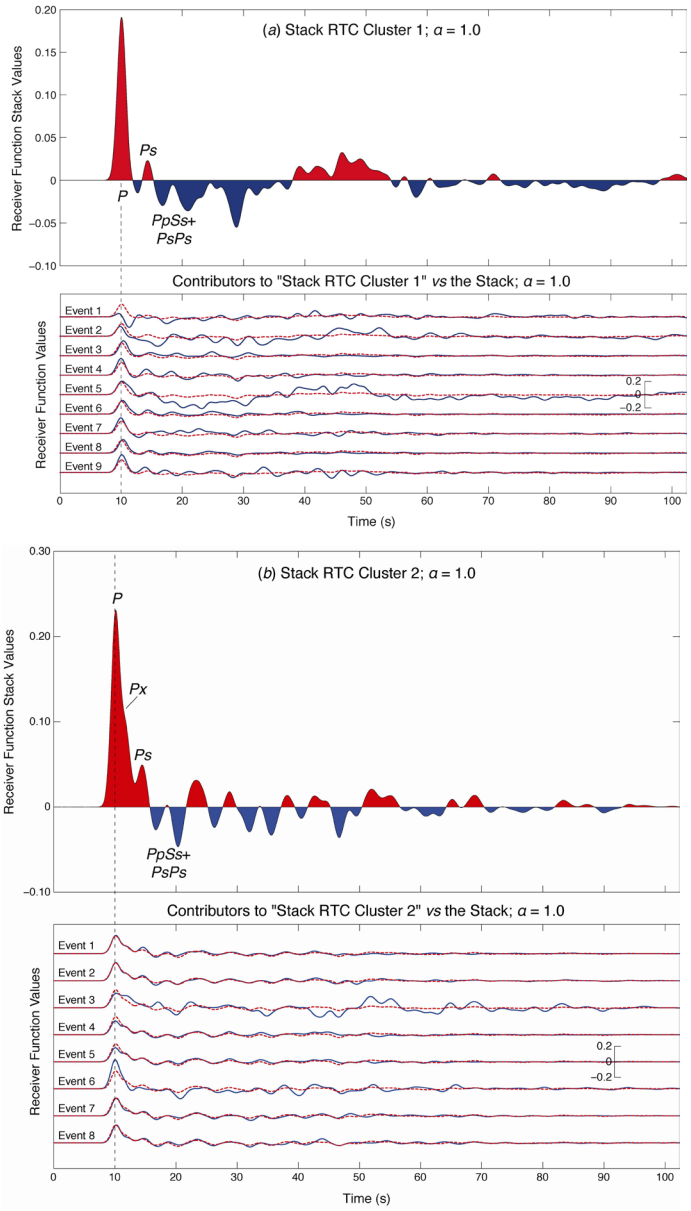

Figure 7. *RTC stacked radial receiver functions (at the top) and their contributors (below) using a Gaussian filter of α = 1 for the (a) southwest and (b) east clusters. Receiver function stacks of each cluster label the prominent parts of the signal.*

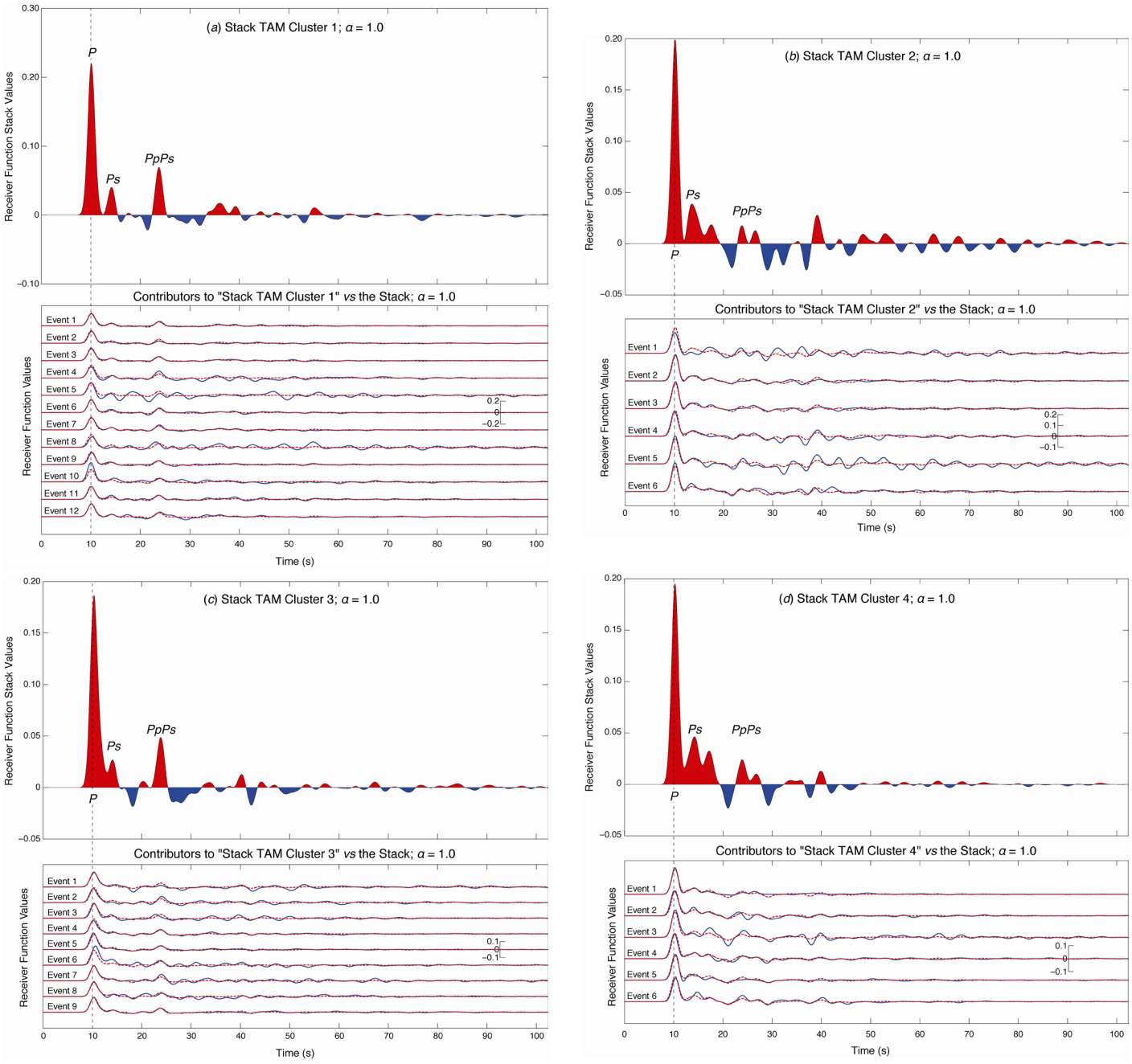

Figure 8. *RTC stacked radial receiver functions (at the top) and their contributors (below) using a Gaussian filter of α = 1 for the (a) southwest and (b) east clusters. Receiver function stacks of each cluster label the prominent parts of the signal.*

receiver function incorporates the direct (*P* wave) and its single (*Ps*) and multiple (e.g., *PpPs* and *PpSs+PsPs*) conversions from discontinuities under each station. The *S* converted phases on Q are deconvolved by using the corresponding *P*-wave and coda on *L*. In this case-study, the percentage of deconvolution (fraction of Q explained by *L*) of each receiver function is computed and no receiver function with less than 70% of the signal reproduced is used.

Inversion of Receiver Functions

In order to obtain the velocity models we seek, we first isolate the receiver functions and then proceed to invert for the velocity model using Herrmann's [2007] approach. In order to reduce the incoherent noise generated by incoming signals, the receiver functions were grouped according to similar backazimuth (±7.5°) and distance (±7.5°) to create clusters of sources. We stack receiver functions from these clusters (by unweighted means) to increase the signal-to-noise ratio and decrease the effects of both ambient and deconvolution noise.

Since the RTC and TAM are too far apart for regional analysis of the crust, we process them independently. We use *P* radial receiver functions with Gaussian filter parameters of $\alpha = 1.0$. These parameters produce the best result (by visual inspection). Figures 6a and 6b show the resulting receiver functions for RTC and TAM.

Results and discussion

In this section we discuss our estimated *S* velocity models of the crustal and upper mantle. Receiver function inversions

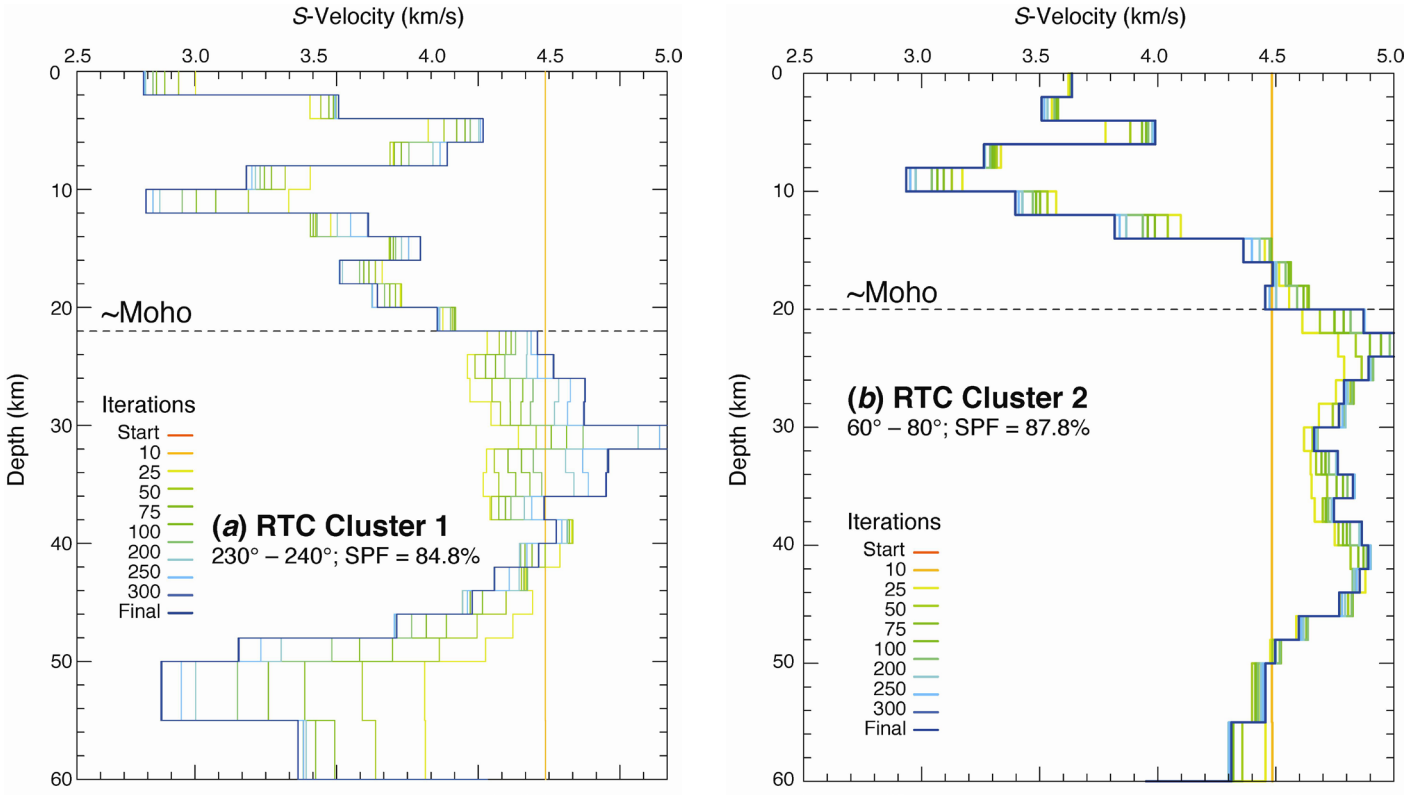

Figure 9: Velocity-depth models of the crust beneath RTC in the western Rabat derived from the stacked receiver functions in Figures 7a and b. Starting model is in orange; blue lines are the final models; other colors are samples of intermediate results during the iterative modeling process. Dashed line shows inferred Moho. SPF is the Signal Power Fit Figure of merit. (a) Modeled from events of source cluster 1 ("C1" in Figure 4a and Table 1.1, spanning backazimuths 60–80°), and (b) modeled from cluster 2 ("C2" and Table 1.2, spanning backazimuths 230–250°)

of the stack (Figures 7 and 8) from each event cluster allow us to obtain several different velocity models for each station (Figures 9 and 10) and we use these to examine the accuracy of the models and possible local variations in structure. To test the robustness of our velocity models, we used several different starting velocity models. We find that for these different initial models the inversion results in the same final velocity models for a given cluster to within the data variance. We conclude that our final velocity models are largely independent of the initial velocity models used. Nevertheless, our final velocity models are reliable only to a depth of about 50 km because resolution weakens and parameters variance grows too large at greater depths.

Crustal structure at RTC

The teleseismic events used for RTC arrive mainly from the northeast (60–80°) and the west (220– 290°) backazimuths (Figure 4a and Table 1). We used only 58 of the ~200 events we examined to create the receiver functions in Figure 6a for RTC. Many of the other seismograms were rejected either because for their low signal to noise ratio or because their deconvolution reproduces less than 70% of the recorded signal.

The direct *P* phases and the direct *Ps* converted phases on Figure 6a (*P*-to-*S* Moho conversions) are clear and distinct. Direct *P* has the largest amplitude of any phase and always correlates in time from one trace to another. We also take note of a very strong phase Px that arrives 1.4–1.5 *s* after the direct *P* for events with eastern backazimuth. These *Px* peaks are likely to be the result of intra-crustal conversions at intermediate interfaces.

Figure 6a shows 52 receiver functions obtained from seismic events that fall in the appropriate distance range and have good signal to noise ratios. Of these, only two clusters of events are compact enough to be selected for stacking at RTC, due to the relatively brief period of recording available. Thus, we identify two source clusters "RTC C1" with nine events to the southwest, and “RTC C2" with eight events to the east (Figure 4a).

The amplitude of the *P*-to-*S* converted phases is weak so we use a stacking process to enhance their signal-to-noise ratio. Thus, the stack of all the receiver functions selected for a given cluster shows the most prominent signal features, though details can be lost. Stack RTC C1 (Figure 7a) contains arrivals from the west. There is one dominant arrival on the stacked trace in the first 4.5 *s* after direct *P*, which we interpret as the Moho *P*-to-S conversion. Stack RTC C2 (Figure 7b) consists of data from more eastern backazimuths. For this stack, peak *Px* is clear, as it is in the contributing receiver functions. Once again, Px is very close to the direct *P*-wave, at about 1.5 *s* after. Additional arrivals appear on this stack but we interpret them as filter bounces.

In Figure 9a, model RTC C1 is generated from events southwest of the station (Figure 4a and Table 1.1) and shows a high velocity layer (4.2 km/s) between 4 and 8 km depth followed by a low velocity zone (2.8 km/s) between 8 and 12 km depth. The velocity then increases gradually from 2.8 km/s

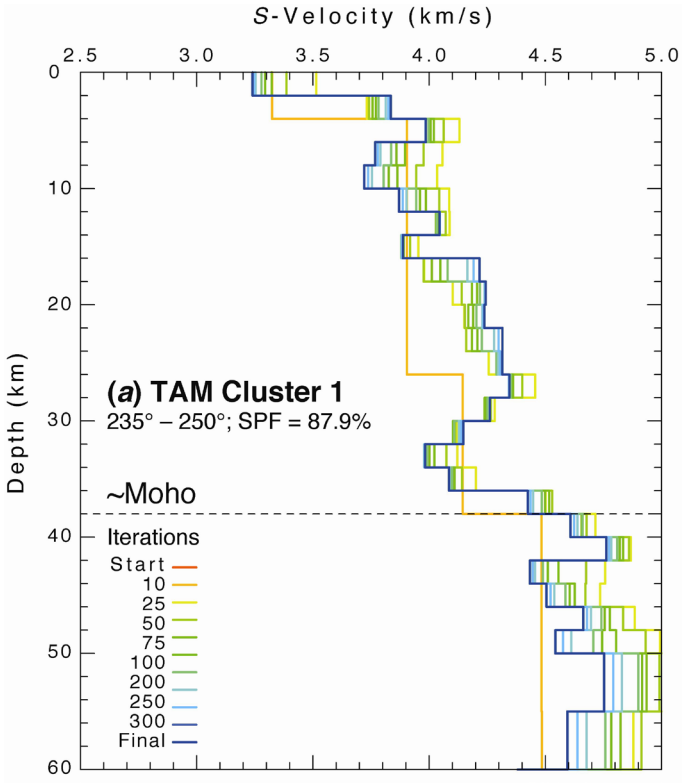
S-Velocity (km/s)
2.5
3.0
3.5
4.0
4.5
5.0
Depth (km)
0
10
20
30
40
50
60
(a) TAM Cluster 1
235° – 250°; SPF = 87.9%
~Moho
Iterations
Start
10
25
50
75
100
200
250
300
Final

A

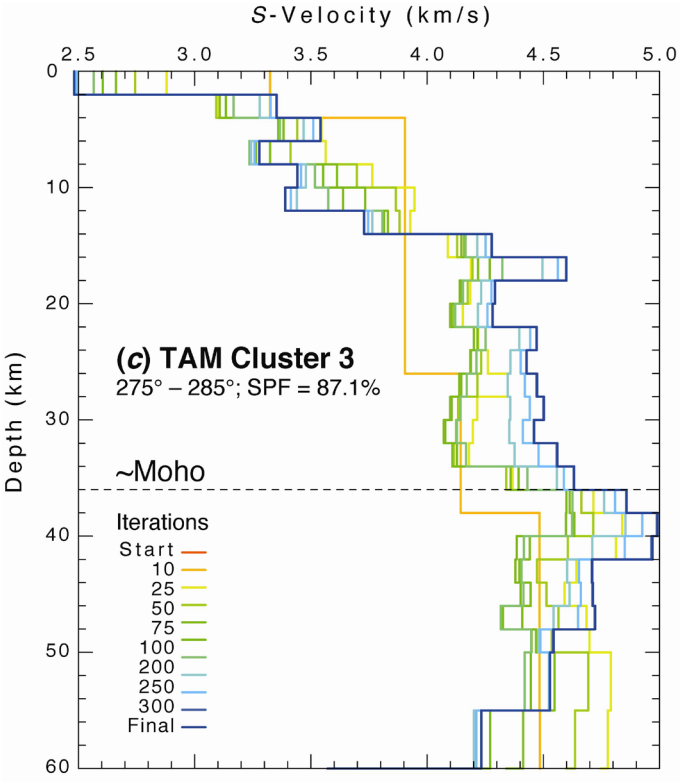
S-Velocity (km/s)
2.5
3.0
3.5
4.0
4.5
5.0
Depth (km)
0
10
20
30
40
50
60
(c) TAM Cluster 3
275° – 285°; SPF = 87.1%
~Moho
Iterations
Start
10
25
50
75
100
200
250
300
Final

C

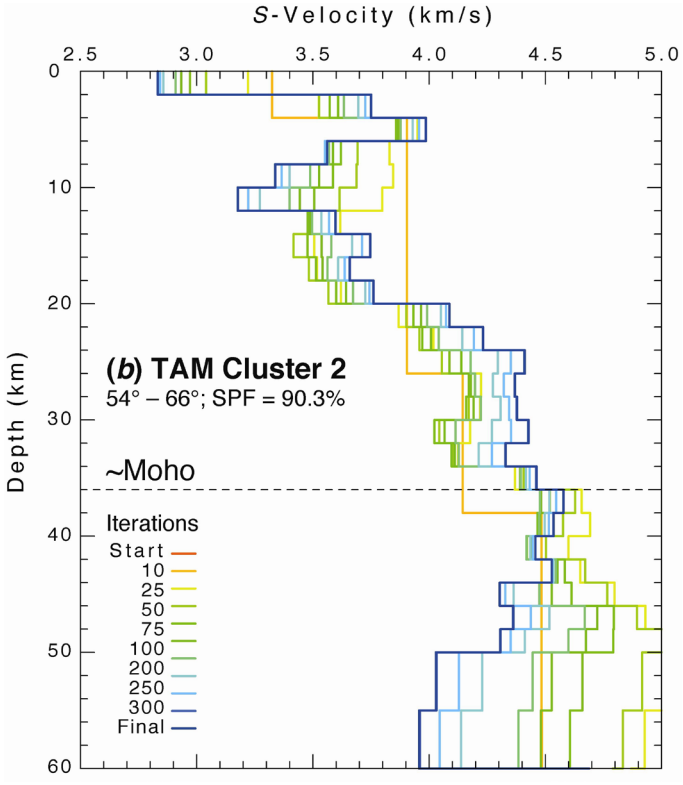
S-Velocity (km/s)
2.5
3.0
3.5
4.0
4.5
5.0
Depth (km)
0
10
20
30
40
50
60
(b) TAM Cluster 2
54° – 66°; SPF = 90.3%
~Moho
Iterations
Start
10
25
50
75
100
200
250
300
Final

B

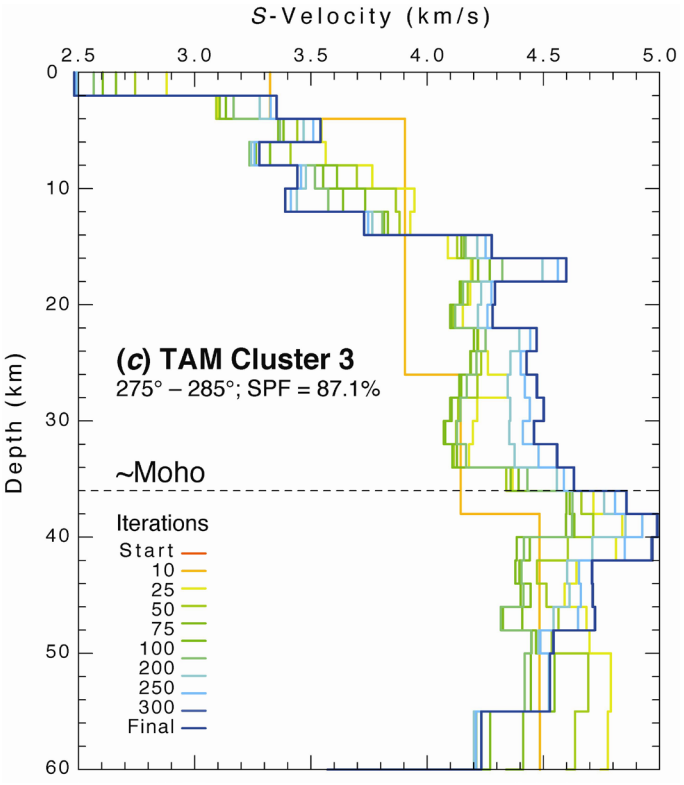
S-Velocity (km/s)
2.5
3.0
3.5
4.0
4.5
5.0
Depth (km)
0
10
20
30
40
50
60
(c) TAM Cluster 3
275° – 285°; SPF = 87.1%
~Moho
Iterations
Start
10
25
50
75
100
200
250
300
Final

D

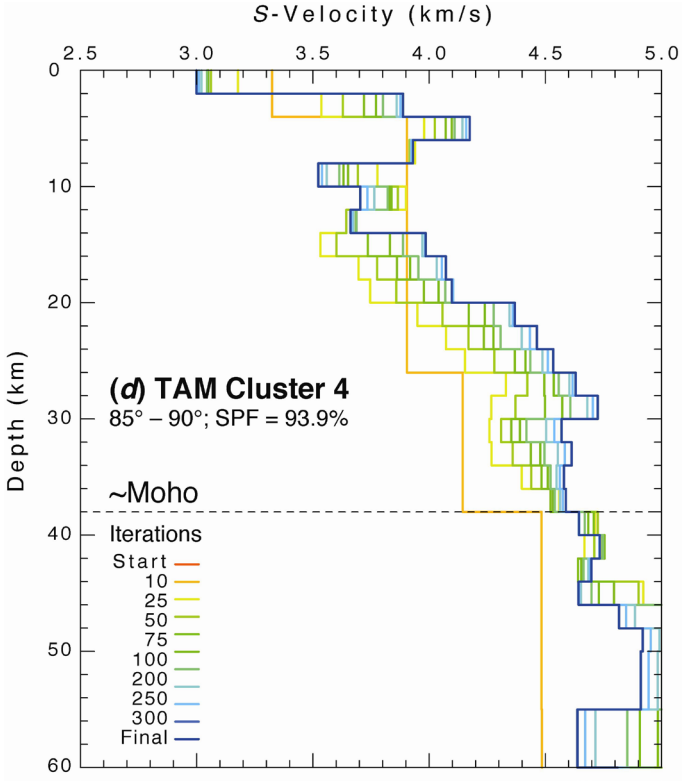

Figure 10: *Models derived from receiver function stacks in Figures 8a–d; format as in Figure 9. The starting model (orange) is the velocity model of Sandvol [1998]. SPF is the Signal Power Fit Figure of merit. (a) Cluster 1 (Figure 8a and Table 2.1), (b) cluster 2 (Figure 8b and Table 2.2), (c) cluster 3 (Figure 8c and Table 2.3), and (d) cluster 4 (Figure 8d and Table 2.4).*

to 4.8 km/s with Moho depth at around 22 km deep.

For the eastern backazimuth, model RTC C2 (Figure 9b and Table 1.2) has a distinct low-velocity layer between 6 and 12 km depth and *S*-velocity as low as 2.9 km/s. Velocity increases gradually with depth and at 20 km reaches Moho, marked by a sharp increase in velocity. Moho does not appear as abrupt at this backazimuth so we conclude that Moho is more gradational east of Rabat than it is to the west, but note that both velocity models RTC C1 and RTC C2 have velocity gradients adjacent to Moho with sharp boundaries accounting for only a fraction of the Moho velocity contrast; finally, there are rather large velocity variations within the crust, implying complexity in crustal structure under RTC. In both models, there is an upper-crustal low-velocity zone (LVZ) between 8 and 12 km. Model C1 has the sharp portion of Moho at a 22 km depth but C2 at 20 km depth (Figures 9a and b).

Thus, the Moho under RTC shallow and gradational, probably reflecting a transitional zone between continental and oceanic crust. Shallow Moho is consistent with geologic and isostasy data, which suggest continental and oceanic Moho at 30 and 15 km near Rabat [29].

Study of exposed Triassic-Jurassic (200 to 65 million years) rifts of the continental margins of eastern North American and West Africa suggests that Atlantic Ocean has been opened by extension during rifting [30]. A slight decrease of crustal thickness is commonly expected in a rift regime as a result of extension. Our observations clearly indicate thinning of the crust (20 – 22 km) below station RTC, in comparison to the eastern area in the continent (30 km). Thus, we conclude that the thinning occurred with extension during this rifting phase.

Crustal structure at TAM

Many more events were available for station TAM. As with RTC, a large number of these are to the east and west (50°–100° and 230°–290° backazimuths) but two additional clusters are available for TAM. We analyzed 92 teleseismic events and selected four clusters (Figure 4b and Table 2). In Figure 6b, direct *P* and *Ps* (*P*-to-S conversion) are quite distinct in the receiver functions. We also see crustal multiples PpPs about 12–14 *s* after the onset of the direct P. We evaluated a receiver-function stack for each group. Cluster "TAM C1" consists of twelve events from the southwest, TAM C2 of six events from the east-northeast, TAM C3 of nine events from the west, and TAM C4 of six events from the southeast.

There is less energy on the receiver function for *P*-to-S and multiple conversions. Receiver functions stacks and theirs contributors for TAM are shown in Figure 8. Stacks from eastern clusters (TAM C2 and TAM C4) are similar enough; both stack TAM C2 and TAM C4 show two twin characteristic peaks. Peak *Ps* is found at about 4.5 *s* and is joined to another peak. The multiple PpPs is also joined to another peak on both stacks. The amplitude of peak *Ps* is more important than the one of PpPs. Stacks from western clusters (TAM C1 and TAM C3) are similar. We observe three main peaks on stack TAM C1 and TAM C3. *P*-to-S conversion at the Moho is found at 4.5 s. Contrary to the eastern stacks, the peaks are single and the amplitude of PpPs is more important than the one of *Ps* on both stacks. These observations provide an evidence for intruding structure east of station TAM.

The inversion results stacked receiver functions of the four event clusters are shown in Figure 10.

Our initial model in orange (Figure 10) comes from Sandvol et al. [6].

The southwest model, TAM C1 (Figure 10a), can be separated into three velocity patterns. The first is a complex pattern dominated by a gradient from the surface to 16 km depth and velocities between 3.2 and 3.9 km/s; its average *S* velocity of about 3.7 km/s. The second is from 16 to 30 km deep and represents the lower crust. It has a roughly constant *S* velocity of ~4.25 km/s and varies between 4.2 and 4.35 km/s. Third is a low-velocity zone from 30 to 38 km depth, with *S-wave* velocities that drop to 4.0 km/s. Moho depth is about 38 km.

The eastern backazimuth, model TAM C2 (Figure 10b), is quite similar to TAM C4, with an upper crust LVZ from 6 to 12 km depth; the lower crust extends from 20 to 36 km depth with a velocity gradient and variations from 4.1 to 4.55 km/s. Moho is at about 36 km and a modest velocity gradient below it implies a transitional style.

The western backazimuth, model TAM C3 (Figure 10c) shows two main velocity zones, one from the surface to 14 km depth, with a complex velocity pattern averaging about 3.4 km/s. The second is between 14 and 36 km depth and has a mild velocity gradient from 4.2 to 4.6 km/s; Moho depth is about 36 km.

Model TAM C4 (Figure 10d; east-northeast backazimuth) has an upper crust characterized by a low velocity zone from 8 to 14 km depth. This LVZ is followed by a velocity gradient which ranges from 3.7 km/s at 14 km depth to 4.1 km/s at 20 km deep. The lower crust extends from 20 to 38 km depth with a gradient in *S* velocity and variations between 4.4 and 4.7 km/s; Moho is

at about 38 km.

Our inversion results are largely consistent between the four clusters. Models TAM C2 and TAM C3 (western and eastern) have Moho at 36 km while models TAM C1 and TAM C4 (southwest and southeast) put the Moho slightly deeper, at 38 km (Figures 10a–d). These results are consistent with those of Doser and Sandvol, who estimate Moho depth at 38±2 km; we infer with some confidence that the thickness of the crust is about 38 km under TAM [23,6].

Our *S* velocity models for TAM show modest low velocity zones in the upper crust. In the upper 2 km, VS varies from 2.5 to 3.5 km/s (Figures 10a and c, TAM C1 and TAM C3). Our models TAM C2 and TAM C4 have distinct high velocity zones between 2 and 8 km depth. This observation directly indicates that there is strong local variation of velocity structures; these may correspond to the high conductivity unit and intrusions east of TAM inferred by Lesquer and Ayadi [18,22]. We assume that, one of the most probable explanations for the LVZ on the eastern velocity models is the existence of a magmatic intrusion. No similar feature is observed west of the station, suggesting that crustal structure changes from east to west of TAM. Mid-crust velocities are quite similar among all four models, with velocity increasing with depth so that it reaches 4.2 to 4.6 km/s around 24 to 28 km depth. In the lower crust, the four models are similar except for TAM C1 (Figure 10a), where there is an LVZ between 28 and 36 km depth. Velocity is gradational from the lower crust to the Moho, and in two cases continuing below Moho — a transitional Moho.

The differences between the four models are attributable to exogenous (externally driven) structures in the crust and upper mantle. Because TAM is installed in a complex portion of a craton (Saharan Metacraton or Hoggar Craton), its stability is affected by thermal and gravity anomalies from magmatic intrusions that influence wave velocity. The four clusters exhibit very similar velocities with enough vertical variation to distinguish upper and lower crust and the upper mantle.

The Mohorovičić discontinuity is 20 to 90 km beneath typical continents, with an average of 35 km. In the Hoggar range, the Panafrican basement (600 MY) is associated with the

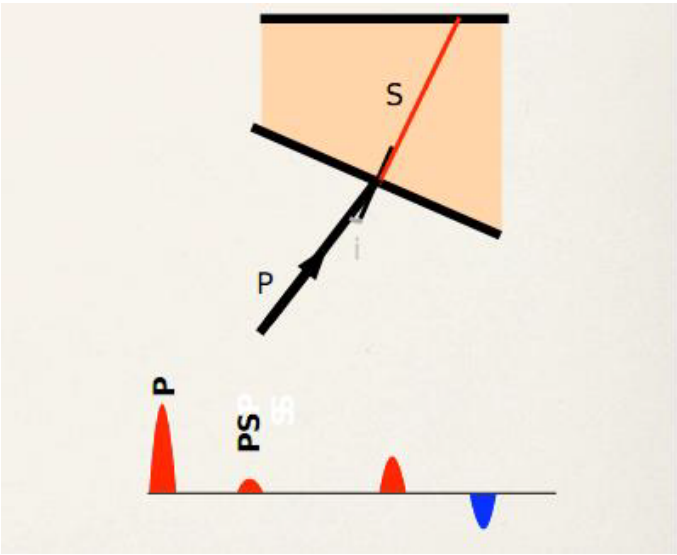

Figure 11: *Synthetic receiver function illustrating the behavior of a wave on an interface inclined with the angle of incidence smaller (Incidence angle small, amplitude of Ps low).*

Panafrican range. The latter has been described as a collision range pinched between a westward lying strong stable craton and a mobile zone further to the east which is considered to be an active margin. The topographic highs uplifted since the Pliocene [31] in the Hoggar, explain the Moho found at 38 km depth, above to the average.

According to the amplitude of *Ps* and *PpPs* peaks, we distinguish two categories of stacks showing a characteristic dissymmetry between the West and East sites of the station:

- The stacks TAM C2 and TAM C4, obtained from eastern of the station are similar; each one shows two twin peaks representing *Ps* and *PpPs* arrivals. Each twin arrival is characterized by the stronger amplitude for the first peak compared with the second one and the amplitude of *Ps* is more important than *PpPs*'s. We think that there is an intra-crustal structure close to the moho, in the path of the *Ps* and *PpPs*.
- Stacks from the west (TAM C1 and TAM C3) are also similar. Contrary to the stacks from East, peaks are simple and the amplitude of *PpPs* is stronger than the one of *Ps*. This can be justified by wave front reaching a dipped Moho (following the principle of Figure 11).

To explain the dissymmetry between the eastern and western stack, we use the figure 3. We note that the faults affect the region following the N-S direction. Because of notable similarity of stacks from each side and the dissymmetry of both side (East and West), we conclude that the faults structures are very deep and can reach the Moho.

Conclusions

We use a time-domain iterative deconvolution method to three-component broadband teleseismic direct *P* and its coda to compute receiver functions for permanent seismic stations RTC and TAM. Two clusters of earthquakes recorded by RTC were compiled and stacked for southwest and east backazimuths and imply velocity-model variations with backazimuth. Our inversion results (receiver function to *S* velocity model) reveal that velocities from the two clusters are similar, excepting differences in velocities and depths near Moho. We find an LVZ between 8 and 12 km depth in both cases. For the southwest backazimuth, we also note large velocity variability indicating crustal complexity toward the ocean. Moho depth beneath RTC is similar between the two backazimuths at about 20 to 22 km. We infer that this shallow Moho results principally from RTC's location in a transition zone between ~30-km thick continental crust to the east and ~15-km thick oceanic crust of the Atlantic margin to the west. Moho is characterized by a velocity gradient; Moho beneath Rabat is of transitional style.

At TAM, far to the east of RTC on Hoggar Craton, receiver function velocity models from four backazimuths imply largely consistent structures. We use starting velocity models from Sandvol [6]. (We also tried a range of different initial velocity models to confirm the robustness of our final models). Near-surface V_S varies between 2.4 and 3.5 km/s; a strong LVZ between 2 and 8 km to the east may correspond to a high-conductivity unit and possible intrusions mentioned in the literature. No similar feature is seen west of the station; suggesting that crustal structure east and west of the station differ (cf., Figure 3). In the mid-crust, the velocity profiles are similar at all backazimuths, with velocity increasing gradationally from 24 and 28 km depth and reaching 4.2 to 4.6 km/s, depending on backazimuth. The models are fairly similar, excepting an LVZ between 28

and 36 km depth in C2, the southwest model. Since increases gradationally in the lower crust and in one instance into the upper mantle, Moho is transitional under TAM as well.

Differences in velocity models between Rabat (RTC) and southern Algeria (TAM) are consistent with their contrasting tectonic environments. RTC velocities are variable and contrast between the two backazimuths; TAM has nearly uniform velocities between its four backazimuths but with enough variation to allowing us to distinguish blocks to the east and west of that station. These results are consistent with TAM's location on a boundary within a stable craton and RTC's thick sediments in an ocean-continent transition zone. This tectonic contrast also is reflected in Moho depth, which is about 20 km beneath RTC but nearly 38 km beneath TAM.

Acknowledgements

We thank the IRIS Data Center for access to data from station RTC and TAM and R. Herrmann for his Receiver function and inversion programs. Thanks to Oscar Gislele Meless (CTBTO/UN Vienna) and Mr. Casmir (ING/CNRST, Morocco) for helpful discussions in the start of this work. Constructive advice by EL Arbi Toto (IBN Tofail University) improved the paper as well. We are grateful to Tsanga Messi Claude Bernard (CBB/Cameroon) and Njikam Seidou (Cameroon Embassy in Morocco) for providing us material.

References

1. Zhu L, Kanamori H. Moho depth variation in southern California from teleseismic receiver functions. J Geophys Res. 2000;105:2969-2980.
2. Langston C. Structure under Mount Rainer Washington, Inferred from teleseismic body waves. J Geophys Res. 1979;84:4749-4762.
3. Langston CA, Isaacs CM. A crustal thickness constraint for central Pennsylvania. Earthquake Notes. 1981;52:13-22.
4. Hebert L, Langston CA. Crustal thickness estimate at AAE (Addis-Ababa, Ethiopia) and NAI (Nairobi, Kenya) using teleseismic P-wave conversions. Tectonophysics. 1985;111:299-327.
5. Angus DA, Wilson DC, Sandvol E, Ni JF. Lithospheric structure of the Arabian and Eurasian collision zone in eastern Turkey from S-wave receiver functions. Geophys J Int. 2006;166:1335-1346. doi:10.1111/j.1365-246X.2006.03070.x.
6. Sandvol E, Dogan S, Alexander C, Muawia B. Grid search modeling of receiver functions: Implications for crustal structure in the Middle East and North Africa. J Geophys Res. 1998;103:26899-26917.
7. Litto W, Jaaidi EB, Medina F, Dakki M. Etude sismo-structurale de la marge nord du bassin du Gharb (avant-pays rifain, Maroc): Mise en évidence d'une distension d'âge miocène tardif. Eclogae Geol Helv. 2001;94:63-73.
8. El Hassani A. Les structures Calédono-Hercyniennes dans la zone de Rabat-Tiflet (Meseta Marocaine septentrionale). Bull Inst Sci Rabat. 1987;11:47-58.
9. Zouhri L, Lamouroux C, Piqué A, Vachard D. La Mamora (Maroc), charnière entre Rharb et Meseta, Conséquences sur la géodynamique. In: 18ème Réunion des Sciences de la Terre; Paris, 2000.
10. Zouhri L. Hétérogénéité des cotes piézométriques et structuration en blocs dans les aquifères côtiers marocains. J Sci Hydrol. 2002;47:969-982.
11. Laville E, Piqué A. La distension crustale atlantique et atlasique au Maroc au début du Mésozoïque: Le rejeu des structures hercyniennes. Bull Soc Géol France. 1991;162:1161-1171.
12. Piqué A, Jeannette D, Michard A. The western Meseta shear zone, a major and permanent feature of the Hercynian belt in Morocco. J Struct Geo. 1979;2:55-61.
13. Piqué A. La zone de Rabat-Tiflet (Méséta marocaine septentrionale), Sa place dans l'ensemble des noyaux paléozoïques de la Méditerranée occidentale. C R Acad Sci Paris. 1982;295:263-266.
14. Ben Sari D. Connaissance géophysique du Maroc [Doctoral thesis]. Université de Grenoble; 1978.
15. Liégeois J-P. The Hoggar swell and volcanism, Tuareg shield, Central Sahara: Intraplate reactivation of Precambrian structures as a result of Alpine convergence. MantlePlumes.org. 2006.
16. Djellit H, Henry B, Deride MEM. Sur la présence d'une série molassique (de type série pourprée) au Sud-Est de l'Ahaggar (In Guezzam, Ahaggar, Algérie). C R Geoscience. 2002;334:789-794.
17. Sleep NH. Hot spots and mantle plumes: Some phenomenology. J Geophys Res. 1990;95:6715-6736.
18. Lesquer A, Bourmatte A, Dautria JM. Deep structure of the Hoggar domal uplift (Central Sahara, south Algeria) from gravity, thermal and petrological data. Tectonophysics. 1988;152:71-87.
19. Fishwick S. Seismic studies of the African continent and a new surface wave model of the uppermost mantle. Paper presented at: Workshop TOPOAFRICA; November 13, 2007; Geosciences Rennes, Rennes, France.
20. Aït-Hamou F, Dautria JM. Le magmatisme cénozoïque du Hoggar: Une synthèse des données disponibles, Mise au point sur l'hypothèse d'un point chaud. Bull Serv Géol Algérie. 1994;5:49-68.
21. Aït-Hamou F, Dautria JM, Cantagrel JM, Dostal J, Briqueu L. Nouvelles données géochronologiques et isotopiques sur le volcanisme cénozoïque de l'Ahaggar (Sahara Algérien): Des arguments en faveur d'un panache. C R Acad Sci Paris. 2000;330:829-836.
22. Ayadi A, Dorbath C, Lesquer A, Bezzeghoud M. Crustal and upper mantle velocity structure of the Hoggar swell (central Sahara, Algeria). Phys Earth Planet Inter. 2000;118:111-123.
23. Doser DI, Keller GR, Harder S, Miller KC. Development of a lithospheric model and geophysical database for North Africa. University of Texas at El Paso, Dept of Geological Sciences; 1996. PL-TR-96-2174.
24. Lesquer A, Vasseur G. Heat-flow constraints on the West African lithosphere structure. Geophys Res Lett. 1992;19:561-564.
25. Lesquer A, Takherist D, Dautria JM, Hadiouche O. Geophysical and petrological evidence for the presence of an anomalous upper mantle beneath the Sahara basins (Algeria). Earth Planet Sci Lett. 1990;96:407-418.
26. Herrmann RB. Computer Programs in Seismology, Version 3.30, 28 November 2004, updated 04 March 2007. Saint Louis University; 2007. Available at: http://www.eas.slu.edu/People/RBHerrmann/ComputerPrograms.html.
27. Vinnik LP. Detection of waves converted from P to SV in the mantle. Phys Earth Planet Inter. 1977;15:39-45.
28. Langston CA, Hammer JK. The vertical component P-wave receiver function. Bull Seismol Soc Am. 2001;91:1805-1819.
29. Van der Bosh JWH. Carte gravimétrique du Maroc. Éditions du service géologique du Maroc; Notes et mémoire; 1969. Scale 1:500 000.
30. Withjack MO, Schlische RW, Olsen PE. Diachronous rifting, drifting, and inversion on the passive margin of Eastern North America: An analog for other passive margins. AAPG Bull. 1998;82(5A):817-835.
31. Azzouni-Sekkala A, Bonin B, Benhallou R, Yahiaoui R, Liégeois JP. Cenozoic alkaline volcanism of the Atakor Massif, Hoggar, Algeria. In: Beccaluva L, Bianchini G, Wilson M, eds. Cenozoic Volcanism in the Mediterranean Area. Geological Society of America Special Paper. Vol. 418; 2007:321-340.